

Identification and tunable optical coherent control of transition-metal spins in silicon carbide

Tom Bosma,^{1,*} Gerrit J. J. Lof,^{1,*} Carmem M. Gilardoni,¹ Olger V. Zwier,¹ Freddie Hendriks,¹ Björn Magnusson,² Alexandre Ellison,² Andreas Gällström,³ Ivan G. Ivanov,³ N. T. Son,³ Remco W. A. Havenith,^{1,4,5} and Caspar H. van der Wal¹

¹*Zernike Institute for Advanced Materials,
University of Groningen, NL-9747AG Groningen, The Netherlands*

²*Norstel AB, Ramshllsvgen 15, SE-602 38 Norrköping, Sweden*

³*Department of Physics, Chemistry and Biology,
Linköping University, SE-581 83 Linköping, Sweden*

⁴*Stratingh Institute for Chemistry, University of Groningen,
NL-9747 AG Groningen, The Netherlands*

⁵*Ghent Quantum Chemistry Group,
Department of Inorganic and Physical Chemistry,
Ghent University, B-9000 Gent, Belgium*

(Dated: Version of December 3, 2024)

Abstract

Color centers in wide-bandgap semiconductors are attractive systems for quantum technologies since they can combine long-coherent electronic spin and bright optical properties. Several suitable centers have been identified, most famously the nitrogen-vacancy defect in diamond. However, integration in communication technology is hindered by the fact that their optical transitions lie outside telecom wavelength bands. Several transition-metal impurities in silicon carbide do emit at and near telecom wavelengths, but knowledge about their spin and optical properties is incomplete. We present all-optical identification and coherent control of molybdenum-impurity spins in silicon carbide with transitions at near-infrared wavelengths. Our results identify spin $S = 1/2$ for both the electronic ground and excited state, with highly anisotropic spin properties that we apply for implementing optical control of ground-state spin coherence. Our results show optical lifetimes below 100 ns and inhomogeneous spin dephasing times near 1 μ s, establishing relevance quantum spin-photon interfacing.

Electronic spins of lattice defects in wide-bandgap semiconductors have come forward as an important platform for quantum technologies¹, in particular for applications that require both manipulation of long-coherent spin and spin-photon interfacing via bright optical transitions. In recent years this field showed strong development, with demonstrations of distribution and storage of non-local entanglement in networks for quantum communication²⁻⁶, and quantum-enhanced field-sensing⁷⁻¹¹. The nitrogen-vacancy defect in diamond is the material system that is most widely used and best characterized for this work^{12,13}. However, its zero-phonon-line (ZPL) transition wavelength (637 nm) is not optimal for integration in standard telecom technology, which uses near-infrared wavelength bands where losses in optical fibers are minimal. A workaround could be to convert photons energies between the emitter-resonance and telecom values¹⁴⁻¹⁶, but making these processes efficient is very challenging.

This situation has been driving a search for similar lattice defects that do combine favorable spin properties with bright emission directly at telecom wavelength. It was shown that both diamond and silicon carbide (SiC) can contain many other spin-active color centers that could have suitable properties^{17,18} (where SiC is also an attractive material for its established position in the semiconductor device industry^{19,20}). However, for many of these color centers detailed knowledge about the spin and optical properties is lacking. In SiC the divacancy²¹⁻²³ and silicon vacancy^{10,24-26} were recently explored, and these indeed show millisecond spin coherence times with bright ZPL transitions closer to the telecom band.

We present here a study of transition-metal impurity defects in SiC, which exist in great variety²⁷⁻³¹. There is at least one case (the vanadium impurity) that has ZPL transitions at telecom wavelengths²⁸, around 1350 nm, but we focus here (directed by availability of lasers in our lab) on the highly-analogous²⁸ molybdenum impurity with ZPLs transitions at 1076 nm (in 4H-SiC) and 1121 nm (in 6H-SiC). Theoretical investigations³², early electron paramagnetic resonance^{28,33} (EPR), and photoluminescence (PL) studies^{34,35} indicate that these transition-metal impurities have promising properties. These studies show that they are deep-level defects that can be in several stable charge states, each with a distinctive value for its electronic spin S and near-infrared optical transitions. Further tuning and engineering possibilities come from the fact that these impurities can be grown in a variety of SiC polytypes (4H, 6H, etc., see Fig. 1a).

Our work is an all-optical study of ensembles of molybdenum impurities in p-type 4H-

SiC and 6H-SiC material. The charge and spin configuration of these impurities, and the defect configuration in the SiC lattice that is energetically favored, was until our work not yet identified with certainty. Our results show that these Mo impurities are in the $\text{Mo}^{5+}(4d^1)$ charge state (we follow here conventional notation²⁸: the label 5+ indicates that of an original Mo atom 4 electrons participate in bonds with SiC and that 1 electron is transferred to the p-type lattice environment). The single remaining electron in the 4d shell gives spin $S = 1/2$ for the ground state and optically excited state that we address. While we will later still discuss how this can be concluded from our measurements, we will assume it as a fact from the start since this simplifies the explanation of our experimental approach.

In addition to this identification of the impurity properties, we explore whether ground-state spin coherence is compatible with optical control. Using a two-laser magneto-spectroscopy method^{23,36,37}, we identify the spin Hamiltonian of the $S = 1/2$ ground state and optically excited state, which behave as doublets with highly anisotropic Landé g-factors. This gives insight in how a situation with only spin-conserving transitions can be broken, and we find that we can use a weak magnetic field to tune that both spin levels of the ground state can be optically coupled to a common excited state level (Λ level scheme). Upon two-laser driving of such Λ schemes, we observe coherent population trapping (CPT, all-optical control of ground-state spin coherence and fundamental to operating quantum memories³⁸). The observed CPT reflects inhomogenous spin dephasing times comparable to that of the SiC divacancy^{23,39} (near $1 \mu\text{s}$). In what follows, we first present our methods and results of single-laser spectroscopy performed on ensembles of Mo impurities in both SiC polytypes. Next, we discuss a two-laser method where optical spin pumping is detected. This allows for characterizing the spin sub-levels in the ground and excited state, and we discuss how it can be extended to controlling spin coherence.

I. MATERIALS AND EXPERIMENTAL METHODS

Both the 6H-SiC and 4H-SiC (Fig. 1a) samples are p-type and doped with Mo. The Mo concentration of the 6H sample was estimated to be between 10^{14} and 10^{16} cm^{-3} , and for 4H between 10^{15} and 10^{17} cm^{-3} . The samples were cooled in a liquid-helium flow cryostat with optical access, which was equipped with a superconducting magnet system. The angle ϕ between the direction of the magnetic field and the c-axis of the crystal could be varied, while

both of these direction are kept orthogonal to the propagation direction of excitation laser beams (see Fig. 1b). All results presented in this work come from photoluminescence (PL) or photoluminescence-excitation (PLE) measurements. The excitation lasers were focused to a $\sim 100 \mu\text{m}$ spot in the sample, where the PL exiting the cryostat was collected with a high-NA lens. A more complete description of experimental aspects is presented in the *Methods* section below.

II. SINGLE-LASER CHARACTERIZATION

For our initial characterization of Mo transitions in 6H-SiC and 4H-SiC we used PL and PLE spectroscopy. For the PL measurements, the emitted light was detected by an FTIR spectrometer. Figure 1c shows the PL emission spectrum of the 6H-SiC sample at 3.5 K, measured using an 892.7 nm Ti:sapphire laser for excitation. From this spectrum the ZPL line of the Mo defect will be studied in detail throughout this work. The shaded region indicate the emission of phonon replicas related to this ZPL³⁵. While we could not perform a detailed analysis, the peak area of the ZPL line in comparison with that of the phonon replicas indicates that the ZPL carries clearly more than a few percent of the full PL emission. Similar PL data from Mo in the 4H-SiC sample, together with a study of the temperature dependence of the PL, can be found in the Supplementary Information⁴⁰.

For a more detailed study of the ZPL of the Mo defects, PLE is used. For PLE measurements, the photon energy of a narrow-line excitation laser is scanned across the ZPL part of the spectrum, while PL of phonon-sideband (phonon-replica) emission is detected by a single-photon counter (Fig. 1b). For the 6H-SiC case, a set of three 1130 nm long-pass filters was used to keep light from the excitation laser from reaching the detector. The inset of Fig. 1c shows the resulting ZPL for Mo in 6H-SiC. We measured the ZPL at 1.1057 eV (1121.3 nm). For 4H-SiC we measured the ZPL at 1.1521 eV (1076.2 nm, see Supplementary Information), which is in close agreement with literature³⁵. Temperature dependence of the PLE from the Mo defects in both 4H-SiC and 6H-SiC can be found in the Supplementary Information.

The width of the ZPL is governed by the inhomogeneous broadening of the electronic transition throughout the ensemble of Mo impurities, which is typically caused by nonuniform strain in the crystal. For Mo in 6H-SiC we observe a broadening of 24 ± 1 GHz FWHM

(full width at half maximum), and 23 ± 1 GHz for 4H-SiC. This inhomogeneous broadening is larger than the electronic spin splittings that we anticipate to be present²⁸, and it thus masks signatures of spin levels in optical transitions between the ground and excited state.

III. TWO-LASER CHARACTERIZATION

In order to characterize the spin-related fine structure of the Mo defects, a two-laser spectroscopy technique was employed^{23,36,37}. We introduce this for the four-level system sketched in Fig. 2a. A laser fixed at frequency f_0 is resonant with one possible transition from ground to excited state ($|g_2\rangle$ to $|e_2\rangle$), and causes PL from a sequence of excitation and emission events. However, if the system decays from the state $|e_2\rangle$ to $|g_1\rangle$, the laser field at frequency f_0 is no longer resonantly driving optical excitations (the system goes dark due to optical pumping). In this situation, the PL is limited by the lifetime of the $|g_1\rangle$ state. Addressing the system with a second laser field, in frequency detuned from the first by an amount δ , counteracts optical pumping into off-resonant energy levels if the detuning δ equals the splitting Δ_g between the ground state sublevels. Thus, for specific two-laser detuning values the PL response of the ensemble will be greatly increased, and this identifies energy spacings between the ground-state and excited state spin sublevels. Notably, this technique also gives clear signal for sublevel splittings that are smaller than the inhomogeneous broadening of the optical transition, and the spectral features now reflect the homogeneous linewidth of optical transitions^{23,39}.

In order to generate the detuned laser, part of the excitation-laser beam for PLE was split off. This secondary beam was passed through an electro-optical modulator (EOM) in which an RF signal generates sidebands of the fundamental laser frequency. Next, one of the first-order sidebands was selected by a Fabry-Pérot cavity, locked to transmitting frequency $f_0 + \delta$. In this way, we generated a secondary (probe) beam detuned by δ from the original (control) beam.

In our measurements a 200 μ W continuous-wave control and probe laser were made to overlap in the sample with linear polarization parallel to the c-axis. For investigating Mo in 6H-SiC the control beam was fixed to the ZPL at 1121.32 nm ($f_{\text{control}} = f_0 = 267.3567$ THz), the probe beam was detuned from f_0 by a variable detuning δ (*i.e.* $f_{\text{probe}} = f_0 + \delta$). In addition, a 100 μ W pulsed 770 nm re-pump laser was focused on the defects to counteract

bleaching of the Mo impurities due to charge-state switching^{23,41,42} (which we observed to only occur partially without re-pump laser). All three lasers were parallel to within 3° inside the sample. A magnetic field was applied to ensure that the spin sublevels are at non-degenerate energies. Finally, we observed that the spectral signatures due to spin show strong broadening above a temperature of ~ 10 K, and we thus performed measurements at 4 K (unless stated otherwise).

Figure 2b shows the dependence of the PLE on the two-laser detuning for the 6H-SiC sample (4H-SiC data in Supplementary Information), for a range of magnitudes of the magnetic field (here aligned close to parallel with the *c*-axis, $\phi = 1^\circ$). Two emission peaks can be distinguished, labeled line L_1 and L_2 . The emission (peak height) by L_2 is much stronger than that of L_1 .

Figure 2c shows the results of a similar measurement with the magnetic field nearly orthogonal to the crystal *c*-axis ($\phi = 87^\circ$). Four spin-related emission signatures are visible, labeled as lines L_1 through L_4 . The position (in two-laser detuning) of all four lines evolves linearly with magnetic field and they emerge from the origin. The slope of all four lines (MHz/mT) is in Fig. 2c smaller than in Fig 2b. In contrast to lines L_1 , L_2 and L_4 , which are peaks in the PLE spectrum, L_3 shows a dip due to suppression of the PLE intensity, further discussed below (and a very small peak feature left of L_1 , at half its detuning, is an artifact that occurs due to leakage of a higher-order sideband of the EOM through the optical cavity).

In order to distinguish the lines at various angles ϕ between the magnetic field and the *c*-axis, we follow how each line evolves with increasing angle. We implemented rotation of the *c*-axis with respect to the magnetic field using an AttoCUBE piezo-actuated goniometer with 7.2 degrees travel (and we kept the optical linear polarization along the *c*-axis). Figure 2d shows that as ϕ increases, L_1 , L_3 , and L_4 move to the left, whereas L_2 moves to the right. Near 86° , L_2 and L_1 cross. At this angle, the left-to-right order of the emission lines is swapped, justifying the assignment of L_1 , L_2 , L_3 and L_4 as in Fig. 2b,c. The Supplementary Information presents further results from two-laser magneto-spectroscopy at intermediate angles ϕ , as well as similar results from the 4H-SiC sample.

IV. ANALYSIS

We will show below here that the results as in Fig. 2 indicate that our Mo impurities have electronic spin $S = 1/2$ for the ground and excited state. This contradicts predictions and interpretations of initial results. Theoretically, it was predicted that the Mo defect in 4H and 6H silicon carbide is in the asymmetric split-vacancy configuration (Mo impurity asymmetrically located inside a Si-C divancy), where it would have a spin $S = 1$ ground state with zero-field splittings of about 3 to 6 GHz^{28,32,35} for the charge state corresponding to the ZPL transitions under study here. However, this should lead to the observation of additional emission lines in our measurements. Particularly, in the presence of a zero-field splitting, we would expect to observe lines emerging from a nonzero detuning corresponding to this zero-field splitting²³. We have measured at zero fields, and up to 21 GHz detuning (see Supplementary Information), but found no more peaks than the four present in Fig. 2b. A splitting larger than 21 GHz would have been visible as splitting of the ZPL in the inset of Fig. 1c, which is not the case. Additionally, a zero-field splitting and corresponding avoided crossings at certain magnetic fields would result in curved behavior for the positions of lines in magneto-spectroscopy. Thus, our observations rule out that there is a zero-field splitting for the ground-state and excited-state spin sublevels. For such cases the effective spin-Hamiltonian⁴³ can only take the form of a Zeeman term

$$H_{g(e)} = \mu_B g_{g(e)} \mathbf{B} \cdot \tilde{\mathbf{S}} \quad (1)$$

with $g_{g(e)}$ the g-factor for the electronic ground (excited) state (assumed positive), μ_B the Bohr magneton, \mathbf{B} the magnetic field vector of an externally applied field, and $\tilde{\mathbf{S}}$ the effective spin vector. The observation of four emission lines can be explained, in the simplest manner, by a system with spin $S = 1/2$ in both the ground and excited state.

Further, analysis of data as in Fig. 2b reveals that the positions (in detuning frequency) of lines L_1 through L_4 relate to each other by a set of sum-rules,

$$\Theta_{L3} = \Theta_{L1} + \Theta_{L2}, \quad (2)$$

$$\Theta_{L4} = 2\Theta_{L1} + \Theta_{L2}. \quad (3)$$

Here Θ_{Ln} denotes the slope of emission line n in Hertz per Tesla. We can thus relate the

emission lines to the energy eigenvalues of the effective spin-Hamiltonian in Eq. 1 by

$$\Theta_{L1} = \frac{\mu_B}{h} g_g, \quad (4)$$

$$\Theta_{L2} = \frac{\mu_B}{h} |g_e - g_g|, \quad (5)$$

$$\Theta_{L3} = \frac{\mu_B}{h} g_e, \quad (6)$$

$$\Theta_{L4} = \frac{\mu_B}{h} (g_e + g_g), \quad (7)$$

where h is Planck's constant.

For such a system, Fig. 3 presents the two-laser optical pumping schemes that correspond to the observed emission lines L_1 through L_4 . Addressing the system with the V-scheme from Fig. 3c leads to increased pumping into a dark ground-state sublevel, since two excited states contribute to decay into the off-resonant energy level while optical excitation out of the other ground-state level is enhanced. This results in reduced emission observed as the PLE dip feature of L_3 . Using Eq. (4)-(7), the ground-state and excited-state g-factors can be determined from the two-laser magneto-spectroscopy data.

Since the emission lines have different slopes for different angles ϕ for the magnetic field direction, we conclude that the g-factor is anisotropic. This observation is consistent with the behavior of similar impurities in silicon carbide²⁸. In this scenario a g-factor g consists of a component g_{\parallel} along the c-axis of the silicon carbide structure and a component g_{\perp} in the basal plane. For any orientation of the magnetic field, the g-factor can then be replaced by an effective factor⁴³

$$g(\phi) = \sqrt{(g_{\parallel} \cos \phi)^2 + (g_{\perp} \sin \phi)^2} \quad (8)$$

Fitting this equation to our data for 4H-SiC and 6H-SiC reveals the angular dependence of the g-factor depicted in figure 4. For Mo in 6H-SiC we find

$$g_{\parallel}^e = 1.20 \pm 0.02, \quad g_{\perp}^e = 0.11 \pm 0.02,$$

$$g_{\parallel}^g = 1.61 \pm 0.02, \quad g_{\perp}^g = 0.000 \pm 0.004.$$

where $g_{g(e)}$ indicates the g-factor for the ground (excited) state. For Mo in 4H-SiC we find

$$g_{\parallel}^e = 1.39 \pm 0.2, \quad g_{\perp}^e = 0.10 \pm 0.02.$$

$$g_{\parallel}^g = 1.87 \pm 0.2, \quad g_{\perp}^g = 0.04 \pm 0.04.$$

These values explain the observation in 6H-SiC that L_2 shifts to the left with decreasing angle ϕ (Fig. 2c) while all other lines shift to the right. As a function of ϕ , the effective g_e factor starts out larger than g_g , but at some point it becomes smaller. Thus, the $|g_e - g_g|$ term in Eq. 5 initially decreases towards zero when rotating the field from orthogonal to parallel to the c-axis.

The reason why diagonal transitions (in Fig. 3 panels a,c), and thus the Λ and V scheme are allowed, can be found in the different behavior for the g_e and g_g g-factors. When the magnetic field direction coincides with the internal quantization axis of the defect, the spin states in both the ground and excited state are given by the basis of the S_z operator, where the z -axis is defined as coinciding with the c-axis. This means that the spin-state overlap for vertical transitions, *e.g.* transitions from $|g_1\rangle$ to $|e_1\rangle$, is unity. In such cases, diagonal transitions are forbidden as the overlap between *e.g.* $|g_1\rangle$ and $|e_2\rangle$ is zero. Tilting the magnetic field away from the internal quantization axis introduces mixing in the spin states. The amount of mixing depends on the g-factor, such that it differs for the ground and excited state. This results in a tunable non-zero overlap for all transitions, allowing all four schemes to be observed (as in Fig. 2b where $\phi = 87^\circ$). This reasoning also explains the suppression of all emission lines except L_2 in Fig. 2b, where the magnetic field is nearly along the c-axis.

V. COHERENT POPULATION TRAPPING

The Λ driving scheme depicted in Fig. 3a, where both ground states are coupled to a common excited state, is of particular interest. In such cases it is possible to achieve all-optical coherent population trapping (CPT)³⁸, which is of great significance in quantum-optical operations that used ground-state spin coherence. This phenomenon occurs when two lasers address a Λ system at exact two-photon resonance. The ground-state spin system is then driven towards a superposition state that approaches $|\Psi_{CPT}\rangle \propto \Omega_2 |g_1\rangle - \Omega_1 |g_2\rangle$ for ideal spin coherence. Here Ω_n is the Rabi frequency for the driven transition from the $|g_n\rangle$ state to the common excited state. Since the system is now coherently trapped in the ground state, the photoluminescence decreases.

In order to study the occupance of CPT, we focus on the two-laser PLE features that result from a Λ scheme. A probe laser with variable detuning from a fixed control laser was scanned across this line with a frequency resolution below 50 kHz, at 200 μ W. The control

laser power was varied between 200 μW and 5 mW. This indeed yields signatures of CPT, as presented in Fig. 5. A clear power dependence is visible: when the control beam power is decreased, the CPT depth decreases. Using a standard model for CPT³⁸, adapted to the case for strong inhomogeneous broadening of the optical transitions³⁹ (see also Suppl. Info.) we extract an inhomogeneous spin dephasing time T_2^* on the order of 1 μs and an optical life time of the excited state below 100 ns (the uncertainty is about a factor 2 due to the high number of fit parameters in an approach that accounts for inhomogeneity of the optical transitions). This observation of CPT also confirms our earlier interpretation of lines L_1 - L_4 , in that it confirms that L_1 results from a Λ scheme. While theoretically possible, detecting CPT in a V pumping scheme is less trivial and beyond the scope of this work.

VI. FURTHER DISCUSSION

Behavior of the g-factor similar to what we observe for Mo has been earlier reported from EPR studies by Baur *et al.* on various transition-metal impurities in SiC²⁸. For several elements, including vanadium and titanium, it was concluded that $g_{\parallel}^g \approx 1.7$ and $g_{\perp}^g = 0$. In all these cases the transition metal has a single electron in its 3d orbital and occupies the substitutional hexagonal (h) Si site. The correspondence with what we observe for the Mo impurity, and that we observe this for p-type SiC host material, strongly suggests that our materials have Mo impurities present as $\text{Mo}^{5+}(4d^1)$ systems residing on a hexagonal h silicon substitutional site. In this case, the molybdenum would be bonded in a tetragonal geometry, sharing four electrons with its nearest neighbors, and the defect is in a singly ionized $+|e|$ charge state.

However, recently Ivády *et al.* proposed the existence of the asymmetric split-vacancy (ASV) defect in SiC based on theoretical work³⁰. An ASV defect in SiC occurs when an impurity occupies the divacancy from an adjacent silicon and carbon vacancy. The local symmetry of this defect is a distorted octahedron with a threefold symmetry axis in which the strong g-factor anisotropy ($g_{\perp} = 0$) may also be present for the $S = 1/2$ state⁴³. Considering six shared electrons for this divacancy environment, the $4d^1$ Mo configuration would now occur for the singly charged $-|e|$ state (which is not plausible for our case given that we have p-type material). Baur *et al.*²⁸ studied this Mo charge state in slightly n-type 6H-SiC and reported a fully isotropic g-factor. This corresponds to Mo on a site with cubic

symmetry (k) in the crystal field⁴³. Furthermore, it was mentioned that Mo^{5+} could not be addressed optically.

We thus propose that Mo^{5+} on a lattice site with cubic symmetry may only be stable in n-type SiC, and that its transitions are possibly optically forbidden. On the other hand, Mo^{5+} in hexagonal symmetry is stable in p-type SiC and optically accessible. As mentioned, the vanadium defect center exhibits properties similar to that of the molybdenum defect in the present work. The fact that several of its known optical transitions lay in the O-band for telecom technology²⁹ makes it very attractive for future studies. Other defect centers with transitions close to telecom wavelengths are tungsten impurities⁴⁴, and the nitrogen-vacancy center in SiC^{45,46} (which exhibits properties analogous to the nitrogen-vacancy center in diamond).

VII. SUMMARY AND OUTLOOK

We have studied ensembles of molybdenum defect centers in 6H and 4H silicon carbide with 1.1521 eV and 1.1057 eV transition energies, respectively. The ground-state and excited-state spin of both defects was determined to be $S = 1/2$ with large g-factor anisotropy. Since this is allowed in hexagonal symmetry, but disallowed in cubic, we find this to be consistent with theoretical descriptions that predict that Mo resides at a hexagonal lattice site in 4H and 6H SiC^{30,32}, and our p-type host environment strongly suggests that this occurs for Mo at a silicon substitutional site. We used the measured insight in the $S = 1/2$ spin Hamiltonians for tuning control schemes where two-laser driving address transitions of a Λ system, and observed CPT for such cases. This demonstrates that the Mo defect and similar transition-metal impurities are promising for quantum information technology. In particular for the vanadium color center, engineered to be in SiC material where it stays in its neutral $\text{V}^{4+}(3d^1)$ charge state, this holds promise for combining spin $S = 1/2$ spin coherence with operation directly at telecom wavelengths.

-
- * These authors contributed equally to this work.
1. Gao, W., Imamoglu, A., Bernien, H. & Hanson, R. Coherent manipulation, measurement and entanglement of individual solid-state spins using optical fields. *Nat. Phot.* **9**, 363 (2015).
 2. Togan, E. *et al.* Quantum entanglement between an optical photon and a solid-state spin qubit. *Nature* **466**, 730 (2010).
 3. Dolde, F. *et al.* High-fidelity spin entanglement using optimal control. *Nat. Commun.* **5**, 3371 (2014).
 4. Klimov, P. V., Falk, A. L., Christle, D. J., Dobrovitski, V. V. & Awschalom, D. D. Quantum entanglement at ambient conditions in a macroscopic solid-state spin ensemble. *Sci. Adv.* **1**, e1501015 (2015).
 5. Hensen, B. *et al.* Loophole-free Bell inequality violation using electron spins separated by 1.3 kilometres. *Nature* **526**, 682–686 (2015).
 6. Kalb, N. *et al.* Entanglement distillation between solid-state quantum network nodes. *Science* **356**, 928–932 (2017).
 7. Budker, D. & Romalis, M. Optical magnetometry. *Nat. Phys.* **3**, 227–234 (2007).
 8. Balasubramanian, G. *et al.* Nanoscale imaging magnetometry with diamond spins under ambient conditions. *Nature* **455**, 648–651 (2008).
 9. Dolde, F. *et al.* Electric-field sensing using single diamond spins. *Nat. Phys.* **7**, 459–463 (2011).
 10. Kraus, H. *et al.* Magnetic field and temperature sensing with atomic-scale spin defects in silicon carbide. *Sci. Rep.* **4**, 5303 (2014).
 11. Bonato, C. *et al.* Optimized quantum sensing with a single electron spin using real-time adaptive measurements. *Nat. Nanotechnol.* **11**, 247–252 (2016).
 12. Dobrovitski, V., Fuchs, G., Falk, A., Santori, C. & Awschalom, D. Quantum control over single spins in diamond. *Annu. Rev. Condens. Matter Phys.* **4**, 23–50 (2013).
 13. Childress, L. & Hanson, R. Diamond NV centers for quantum computing and quantum networks. *MRS Bull* **38**, 134–138 (2013).
 14. Radnaev, A. *et al.* A quantum memory with telecom-wavelength conversion. *Nat. Phys.* **6**, 894–899 (2010).
 15. Zaske, S. *et al.* Visible-to-telecom quantum frequency conversion of light from a single quantum

- emitter. *Phys. Rev. Lett.* **109**, 147404 (2012).
16. Dréau, A., Tchekorava, A., Mahdaoui, A. E., Bonato, C. & Hanson, R. Quantum frequency conversion to telecom of single photons from a nitrogen-vacancy center in diamond. *preprint arXiv:1801.03304* (2018).
 17. Weber, J. *et al.* Quantum computing with defects. *Proc. Natl. Acad. Sci. U.S.A.* **107**, 8513 (2010).
 18. Weber, J. *et al.* Defects in SiC for quantum computing. *J. Appl. Phys.* **109**, 102417 (2011).
 19. Friedrichs, P., Kimoto, T., Ley, L. & Pensl, G. *Silicon Carbide*, vol. 1 (Wiley, Weinheim, 2010).
 20. Song, B.-S., Yamada, S., Asano, T. & Noda, S. Demonstration of two-dimensional photonic crystals based on silicon carbide. *Opt. Express* **19**, 11084–11089 (2011).
 21. Koehl, W. F., Buckley, B. B., Heremans, F. J., Calusine, G. & Awschalom, D. D. Room temperature coherent control of defect spin qubits in silicon carbide. *Nature* **479**, 84–87 (2011).
 22. Christle, D. J. *et al.* Isolated electron spins in silicon carbide with millisecond coherence times. *Nat. Mater.* **14**, 160 (2015).
 23. Zwier, O. V., O’Shea, D., Onur, A. R. & van der Wal, C. H. All-optical coherent population trapping with defect spin ensembles in silicon carbide. *Sci. Rep.* **5**, 10931 (2015).
 24. Riedel, D. *et al.* Resonant addressing and manipulation of silicon vacancy qubits in silicon carbide. *Phys. Rev. Lett.* **109**, 226402 (2012).
 25. Kraus, H. *et al.* Room-temperature quantum microwave emitters based on spin defects in silicon carbide. *Nat. Phys.* **10**, 157 (2014).
 26. Widmann, M. *et al.* Coherent control of single spins in silicon carbide at room temperature. *Nat. Mater.* **14**, 164 (2015).
 27. Hobgood, H. M. *et al.* Semi-insulating 6H-SiC grown by physical vapor transport. *Appl. Phys. Lett.* **66**, 1364 (1995).
 28. Baur, J., Kunzer, M. & Schneider, J. Transition metals in SiC polytypes, as studied by magnetic resonance techniques. *Phys. Status Solidi A* **162**, 153–172 (1997).
 29. Magnusson, B. & Janzén, E. Optical characterization of deep level defects in SiC. In *Mater. Sci. Forum*, vol. 483, 341–346 (Trans Tech Publ, 2005).
 30. Ivády, V., Gällström, A., Son, N. T., Janzén, E. & Gali, A. Asymmetric Split-Vacancy Defects in SiC Polytypes: A Combined Theoretical and Electron Spin Resonance Study. *Phys. Rev.*

- Lett.* **107**, 195501 (2011).
31. Koehl, W. F. *et al.* Resonant optical spectroscopy and coherent control of Cr⁴⁺ spin ensembles in SiC and GaN. *Phys. Rev. B* **95**, 035207 (2017).
 32. Csóré, A., Gällström, A., Janzén, E. & Gali, Á. Investigation of Mo Defects in 4H-SiC by Means of Density Functional Theory. In *Mater. Sci. Forum*, vol. 858, 261–264 (Trans Tech Publ, 2016).
 33. Dombrowski, K. *et al.* Identification of molybdenum in 6H-SiC by magnetic resonance techniques. *Phys. Rev. B* **54**, 7323 (1996).
 34. Kimoto, T., Nakajima, T., Matsunami, H., Nakata, T. & Inoue, M. Formation of semi-insulating 6H-SiC layers by vanadium ion implantations. *Appl. Phys. Lett.* **69**, 1113 (1996).
 35. Gällström, A., Magnusson, B. & Janzén, E. Optical identification of Mo related deep level defect in 4H and 6H SiC. In *Mater. Sci. Forum*, vol. 615, 405–408 (Trans Tech Publ, 2009).
 36. Manson, N. & Wei, C. Transient hole burning in NV centre in diamond. *J. Lumin.* **58**, 158–160 (1994).
 37. Santori, C. *et al.* Coherent population trapping in diamond NV centers at zero magnetic field. *Opt. Express* **14**, 7986–7994 (2006).
 38. Fleischhauer, M., Imamoglu, A. & Marangos, J. P. Electromagnetically induced transparency: Optics in coherent media. *Rev. Mod. Phys.* **77**, 633 (2005).
 39. Zwier, O. V. *Two-laser spectroscopy and coherent manipulation of color-center spin ensembles in silicon carbide*. Zernike Institute PhD thesis series, ISSN 1570-1530 (University of Groningen, 2016).
 40. Supplementary Information available upon request (2018).
 41. Beha, K., Batalov, A., Manson, N. B., Bratschitsch, R. & Leitenstorfer, A. Optimum photoluminescence excitation and recharging cycle of single nitrogen-vacancy centers in ultrapure diamond. *Phys. Rev. Lett.* **109**, 097404 (2012).
 42. Wolfowicz, G. *et al.* Optical charge state control of spin defects in 4H-SiC. *Nat. Commun.* **8**, 1876 (2017).
 43. Abragam, A. & Bleaney, B. *Electron Paramagnetic Resonance Of Transition Ions*. International series of monographs on physics (Clarendon Press, Oxford, 1970).
 44. Gällström, A. *et al.* Optical identification and electronic configuration of tungsten in 4H-and 6H-SiC. *Phys. B* **407**, 1462–1466 (2012).

45. Zargaleh, S. *et al.* Evidence for near-infrared photoluminescence of nitrogen vacancy centers in 4 H-SiC. *Phys. Rev. B* **94**, 060102 (2016).
46. Von Bardeleben, H. *et al.* NV centers in 3 C, 4 H, and 6 H silicon carbide: A variable platform for solid-state qubits and nanosensors. *Phys. Rev. B* **94**, 121202 (2016).

Methods

Cryostat During all measurements, the sample was mounted in an Oxford Instruments Spectromag SM4000 flow cryostat with optical access through four windows and equipped with a superconducting magnet system.

Photoluminescence (PL) The PL spectrum was measured by exciting the defects using an 892.7 nm laser for Mo in 6H-SiC and a 514.5 nm laser for Mo in 4H-SiC. The PL was resolved using an FTIR spectrometer.

Photoluminescence Excitation (PLE) The PLE spectrum was measured by exciting the defects using a Toptica DL pro diode laser tunable from 1178 nm to 1158 nm with linewidth below 300 kHz, stabilized within 1 MHz using feedback from a HighFinesse WS-7 wavelength meter. Polarization was linear along the sample c-axis. The laser spot diameter was $\sim 100 \mu\text{m}$ at the sample. The excitation laser was filtered from the emitted PL using a set of three 1130 nm longpass filters. PLE was measured using an ID230 single photon counter. Additionally, to counter charge state switching of the defects, a 770 nm re-pump beam from a Coherent Chameleon Ultra tunable pulsed Ti:sapphire laser was focussed at the same region in the sample. Laser powers as mentioned in the main text.

Two-laser characterization The PLE setup described above was modified by splitting off part of the stabilized diode laser beam. The split-off beam was coupled into a single mode fiber and passed through a Photline NIR-MPX-LN-05 Electro Optic Modulator in which an RF signal from a Rohde & Schwarz SMB 100A signal generator modulated the phase. Several sidebands are created next to the fundamental laser frequency, the spacing of these sidebands was determined by the RF frequency. Next, a Thorlabs SA200-8B Fabry-Pérot Interferometer was used to filter out the unwanted sidebands, transmitting a single first order sideband. The resulting beam was focussed on the same region in the sample as the original PLE beams (diode laser and re-pump) with similar spot size and polarization along

the sample c-axis. Laser powers as mentioned in the main text.

Acknowledgements

We thank A. Gali for discussions and M. de Roos, J. G. Holstein, T. J. Schouten and H. Adema for technical support. Early discussions with Prof. Erik Janzén leading to initiation of this study are gratefully acknowledged. Financial support was provided by ERC Starting Grant 279931, the Zernike Institute BIS program, and the Swedish Research Council grants VR 2016-04068 and VR 2016-05362.

Author Contributions

The project was initiated by C.H.W., O.V.Z, I.G.I and N. T. S. SiC materials were grown and prepared by A.E. and B.M. Experiments were performed by T.B., G.J.J.L. and O.V.Z, except for the PL measurements which were done by A.G. and I.G.I. Data analysis was performed by T.B., G.J.J.L., C.G., O.V.Z., F.H., R.W.A.H. and C.H.W. T.B., G.J.J.L. and C.H.W. had the lead on writing the paper. All authors read and commented on the manuscript.

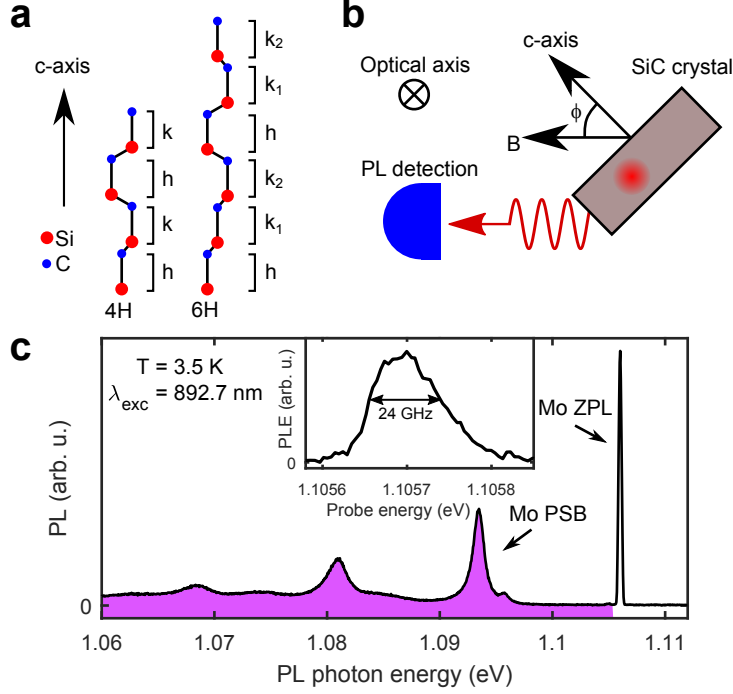


FIG. 1: **Crystal structures of SiC, setup schematic and optical signatures of Mo in 6H-SiC.** **a**, Schematic illustrating the shifts of Si and C layers in the crystal structure of the 4H-SiC and 6H-SiC polytypes, which gives lattice sites with cubic and hexagonal symmetry as labeled by $k_{(1,2)}$ and h , respectively. Our work revisits the question whether Mo impurities are present as substitutional atoms or residing inside Si-C divacancies. The c-axis coincides with the growth direction. **b**, Schematic of SiC crystal in the setup. The crystal is placed in a cryostat with optical access. Laser excitation beams are incident on a side facet of the SiC crystal and propagate along the optical axis (see label), normal to the c-axis. Magnetic fields B are applied in a direction orthogonal to the optical axis and at angle ϕ with the c-axis. Photoluminescence (PL) is detected out of another side facet of the SiC crystal. **c**, PL from Mo in 6H-SiC at 3.5 K and zero field, resulting from excitation with an 892.7 nm Ti:sapphire laser, with labels identifying the zero-phonon-line (ZPL, at 1.1057 eV) emission and phonon replicas (marked as shaded region and labeled as phonon side band, PSB). The inset shows the ZPL as measured by photoluminescence excitation (PLE). Here, the excitation laser is scanned across the ZPL peak and emission from the PSB is used for detection.

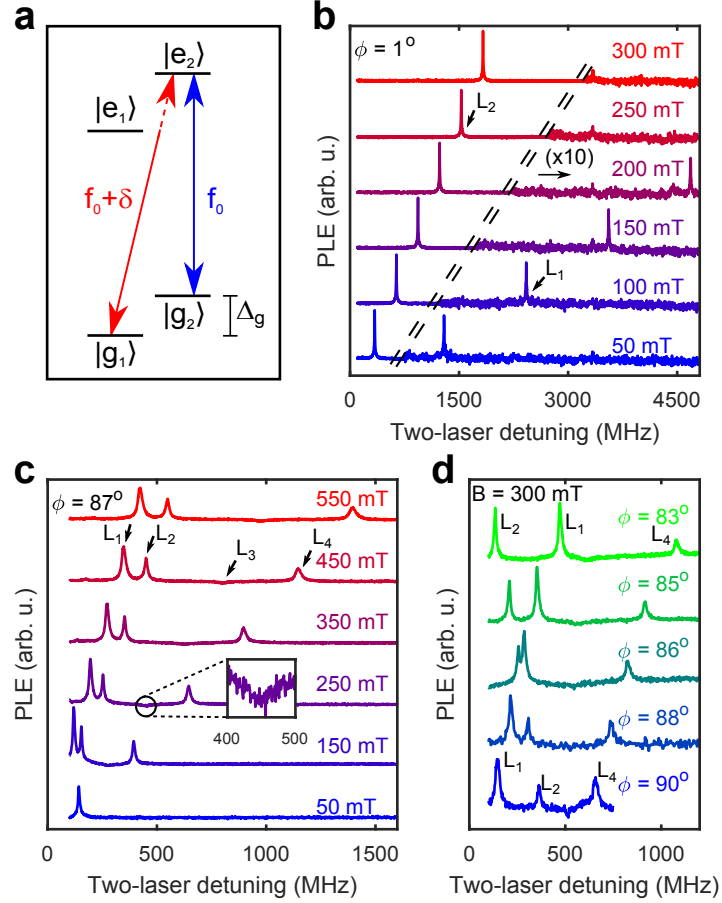


FIG. 2: **Two-laser spectroscopy results for Mo in 6H-SiC.** **a**, Working principle of two-laser spectroscopy: one laser at frequency f_0 is resonant with the $|g_2\rangle$ - $|e_2\rangle$ transition, the second laser is detuned from the first laser by δ . If δ is such that the second laser becomes resonant with another transition (here sketched for $|g_1\rangle$ - $|e_2\rangle$) the photoluminescence will increase since optical spin-pumping by the first laser is counteracted by the second and vice versa. **b-d**, Photoluminescence excitation (PLE) signals as function of two-laser detuning at 4 K. **b**, Magnetic field dependence with field parallel to the c -axis ($\phi = 1^\circ$). For clarity, data in the plot has been magnified by a factor 10 right of the dashed line. Two peaks are visible, labeled L_1 and L_2 (the small peak at 3300 MHz is an artefact from the Fabry-Pérot interferometer in the setup). **c**, Magnetic field dependence with the field nearly perpendicular to the c -axis ($\phi = 87^\circ$). Three peaks and a dip (enlarged in the inset) are visible. These four features are labeled L_1 through L_4 . The peak positions as a function of field in **b-c** coincide with straight lines through the origin (within 0.2% error). **d**, Angle dependence of the PLE signal at 300 mT. Peaks L_1 and L_4 move to the left with increasing angle, whereas L_2 moves to the right. The data in **b-d** are offset vertically for clarity.

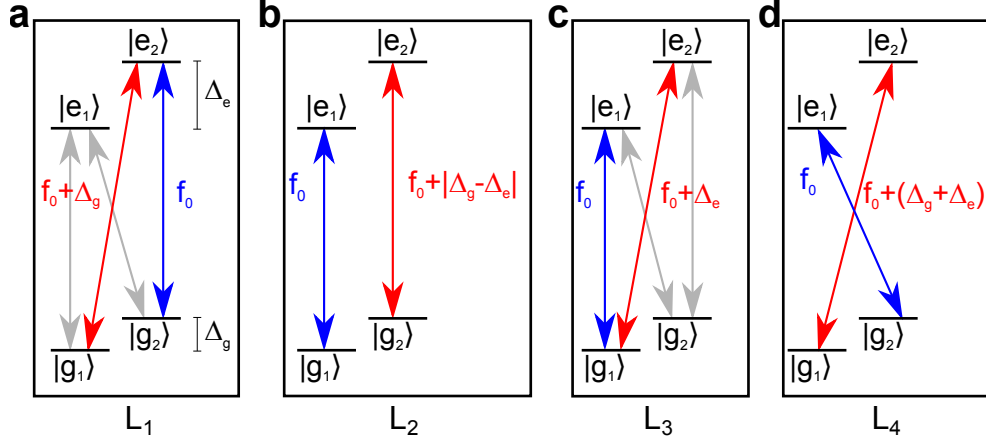


FIG. 3: **Two-laser pumping schemes with optical transitions between $S = 1/2$ ground and excited states.** **a**, Λ scheme, responsible for L_1 emission feature: Two lasers are resonant with transitions from both ground states $|g_1\rangle$ (red arrow) and $|g_2\rangle$ (blue arrow) to a common excited state $|e_2\rangle$. This is achieved when the detuning equals the ground state splitting Δ_g . The gray arrows indicate a secondary Λ scheme via $|e_1\rangle$ that is simultaneously driven in an ensemble when it has inhomogeneous values for its optical transition energies. **b**, Π scheme, responsible for L_2 emission feature: Two lasers are resonant with both vertical transitions. This occurs when the detuning equals the difference between the ground state and excited state splittings, $|\Delta_g - \Delta_e|$. **c**, V scheme, responsible for L_3 emission feature: Two lasers are resonant with transitions from a common ground state $|g_1\rangle$ to both excited states $|e_1\rangle$ (blue arrow) and $|e_2\rangle$ (red arrow). This occurs when the laser detuning equals the excited state splitting Δ_e . The gray arrows indicate a secondary V scheme that is simultaneously driven when the optical transition energies are inhomogeneously broadened. **d**, X scheme, responsible for the L_4 emission feature: Two lasers are resonant with the diagonal transitions in the scheme. This occurs when the detuning is equal to the sum of the ground state and the excited state splittings, $(\Delta_g + \Delta_e)$.

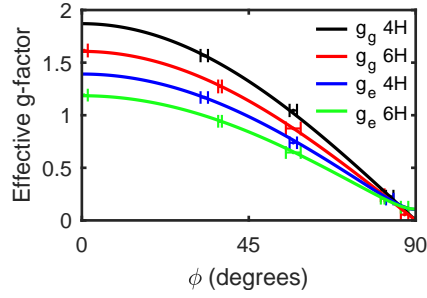


FIG. 4: **Effective g-factors for the spin of Mo impurities in SiC.** Angular dependence of the g-factor for the $S = 1/2$ ground (g_g) and excited states (g_e) of the Mo impurity in 4H-SiC and 6H-SiC. The solid lines indicate fits of Eq. (8) to the data points extracted from two-laser magneto-spectroscopy measurements as in Fig. 2b,c.

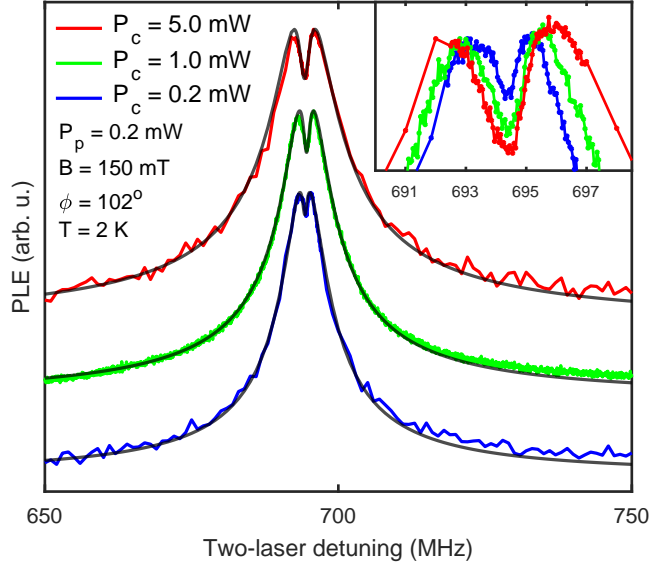


FIG. 5: **Signatures of coherent population trapping of Mo spin states in 6H-SiC.** Two-laser spectroscopy of the L_1 peak in the PLE signals reveals a dipped structure in the peak at several combinations of probe-beam and control-beam power. This results from coherent population trapping (CPT) upon Λ -scheme driving. Temperature, magnetic field orientation and magnitude, and laser powers, were as labeled. The data are offset vertically for clarity. Solid lines are fits of a theoretical model of CPT. The inset shows the normalized feature depths.